

# Unconventional Mechanisms in Niobium Tungsten Oxides for High-rate Lithium-ion Charge Storage

Kent J. Griffith<sup>1</sup>, Kamila M. Wiaderek<sup>2</sup>, Giannantonio Cibirin<sup>3</sup>, Lauren E. Marbella<sup>1</sup>, Clare P. Grey<sup>1\*</sup>

<sup>1</sup>Department of Chemistry, University of Cambridge, Lensfield Road, Cambridge CB2 1EW, UK.

<sup>2</sup> X-ray Science Division, Advanced Photon Source, Argonne National Laboratory, Argonne, IL 60439, USA.

<sup>3</sup> Diamond Light Source, Harwell Science and Innovation Campus, Didcot, Oxfordshire OX11 0DE, U.K.

\*Correspondence to: [cpg27@cam.ac.uk](mailto:cpg27@cam.ac.uk)

The maximum power output and minimum charging time of a lithium-ion battery – key parameters for its use in, for example, transportation applications – depend on mixed ionic–electronic diffusion. While the discharge/charge rate and capacity can be tuned by varying the composite electrode structure, ionic transport within the active particles represents a fundamental limitation. Thus, to achieve high rates, particles are frequently reduced to nanosize dimensions despite this being disadvantageous in terms of volumetric packing density as well as cost, stability, and sustainability considerations. As an alternative to nanoscaling, we show that complex niobium tungsten oxides with topologically frustrated polyhedral arrangements and dense  $\mu\text{m}$ -scale particle morphologies can rapidly and reversibly intercalate large quantities of lithium. Multielectron redox, buffered volume expansion, and extremely fast lithium transport approaching that of a liquid lead to extremely high volumetric capacities and rate performance for both crystallographic shear structure and bronze-like niobium tungsten oxides. The active materials  $\text{Nb}_{16}\text{W}_5\text{O}_{55}$  and  $\text{Nb}_{18}\text{W}_{16}\text{O}_{93}$  offer new strategies toward designing electrodes with advantages in energy density, scalability, electrode architecture/complexity and cost as alternatives to the state-of-the-art high-rate anode material  $\text{Li}_4\text{Ti}_5\text{O}_{12}$ . The direct measurement of solid-state lithium diffusion coefficients ( $D_{\text{Li}}$ ) with pulsed field gradient NMR demonstrates room temperature  $D_{\text{Li}}$  values of  $10^{-12}$ – $10^{-13} \text{ m}^2\cdot\text{s}^{-1}$  in the niobium tungsten oxides, which is several orders-of-magnitude faster than typical electrode materials and corresponds to a characteristic diffusion length of  $\sim 10 \mu\text{m}$  for a 1 minute discharge. Materials and mechanisms that enable lithiation of  $\mu\text{m}$  particles in minutes have implications for high power applications, fast charging devices, all-solid-state batteries, and general approaches to electrode design and material discovery.

New high-rate lithium-ion battery electrode materials that can store large quantities of charge in a few minutes, rather than hours, are required to increase the power and decrease the charging time to help alleviate technological challenges associated with the adoption of electric vehicles and grid-scale batteries, and to enable new power-intensive devices. The most intuitive and commonly used approach to increase the rate performance is to create nanosized or porous (and often hierarchical) structures, which minimize  $\text{Li}^+$  solid-state diffusion distances, enable more rapid  $\text{Li}^+$  transport through the composite electrode and increase the surface areas of electrode materials in contact with electrolyte. Carbonaceous hierarchical structures and carbon-coating are also frequently employed to improve electronic conductivity, which is another prerequisite for the application of high current densities.

In practice, despite excellent lithium mobility, graphite cannot be used at high-rates due to particle fracture and the risk that Li dendrites form, leading to short circuits and potentially fires and explosions<sup>1–3</sup>. The latter issue inherently limits the use of low voltage anodes in high-rate applications, since the electrode inhomogeneity or any source of increased overpotential can lead to Li plating potentials on the surface of the electrode<sup>3</sup>.  $\text{Li}_4\text{Ti}_5\text{O}_{12}$ , with an average voltage of 1.55 V (Fig. S1), enables high-rate (de)intercalation without the risk of Li dendrites or substantial solid–electrolyte interphase (SEI) formation albeit with an undesirable but necessary decrease in full-cell voltage and thus energy density. In this well-established “high”-voltage/high-rate anode, the capacity of 1  $\mu\text{m}$  particles from solid-state synthesis reaches only 60–65  $\text{mA}\cdot\text{h}\cdot\text{g}^{-1}$  at a rate of 10C<sup>4</sup>, where C-rate is defined as the inverse of the number of hours to reach a defined theoretical capacity *e.g.*, 10C corresponds to a 6 min discharge or charge time (see Methods). In contrast, through two decades of research, present carbon-coated nanoparticles of LTO can reach at least 150  $\text{mA}\cdot\text{h}\cdot\text{g}^{-1}$  at 10C,<sup>5,6</sup> 150  $\text{mA}\cdot\text{h}\cdot\text{g}^{-1}$  corresponding to approximately 0.5 lithium ions per transition metal ( $\text{Li}^+/\text{TM}$ ). However, using nano- and porous materials for electrochemical energy storage applications inherently results in a severe penalty in terms of volumetric energy density. Furthermore, these carefully designed porous and nano-architectures are time consuming and expensive to synthesize, characterize, and manufacture, synthesis methods often resulting in relatively low yields and/or the generation of large quantities of chemical waste<sup>7</sup> while also unfortunately being more susceptible to degradation during electrochemical cycling (from processes such as *e.g.* catalytic decomposition of electrolyte,<sup>8</sup> morphological changes that result in loss of nanostructuring,<sup>9</sup> and higher first cycle capacity loss<sup>10</sup>).

In this work, we break from the conventional strategy of nanoscaling and nanostructuring of electrode materials to overcome poor diffusion and electronic properties (found in *e.g.*,  $\text{TiO}_2$  and LTO), and demonstrate that, with the appropriate host lattice, strictly none of the usual criteria discussed above are required to achieve a practical high-rate battery electrode. Instead we leverage insight obtained from prior investigations of complex binary niobium oxides such as T- $\text{Nb}_2\text{O}_5$ <sup>11</sup> and of superionic conductors such as lithium lanthanum titanate (LLTO) perovskite<sup>12</sup>, to identify structural motifs that should exhibit favorable Li diffusion properties, and thus exhibit superior performance, allowing micrometer-sized particles to be used at extremely high rates. We show that when multi-redox 4d and 5d transition metals are used with the appropriate three-dimensional oxide structure, we can achieve extremely high volumetric energy densities and impressive rates. The bulk compounds studied are a series of complex “block” or “bronze-like” oxide structures (Fig. 1) largely comprised of corner- and edge-sharing  $\text{NbO}_6$  and  $\text{WO}_6$  octahedra, both oxides prepared via gram-scale solid-state synthesis. The unusual electrochemical performance is first illustrated by studying large (3–10  $\mu\text{m}$  primary, 10–30  $\mu\text{m}$  agglomerate) dense particles of the

block structure  $\text{Nb}_{16}\text{W}_5\text{O}_{55}$  (Fig. 1a–c). On a mass normalized basis, the lithium storage performance of  $\text{Nb}_{16}\text{W}_5\text{O}_{55}$  exceeds nanostructured versions of heavily studied  $\text{Li}_4\text{Ti}_5\text{O}_{12}$ <sup>5,13–15</sup>,  $\text{TiO}_2(\text{B})$ <sup>16–18</sup>, and  $\text{T-Nb}_2\text{O}_5$ <sup>19–21</sup> under similar loading conditions. Given the high density of the crystal structure and the high tap density of bulk  $\text{Nb}_{16}\text{W}_5\text{O}_{55}$  vs. nanomaterials, this leads to exceptionally high volumetric performance. We further demonstrate the generality of this bulk phenomenon by exploring another new electrode material, bronze-like  $\text{Nb}_{18}\text{W}_{16}\text{O}_{93}$  (Fig. 1d–f).

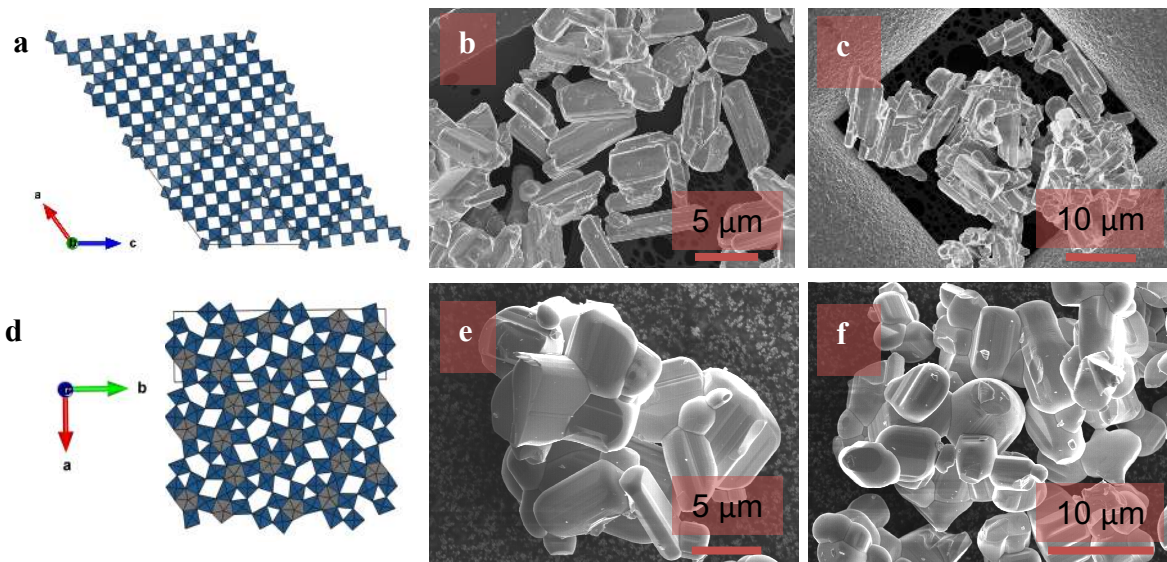


**Figure 1 | Crystal structure and particle morphology of  $\text{Nb}_{16}\text{W}_5\text{O}_{55}$  and  $\text{Nb}_{18}\text{W}_{16}\text{O}_{93}$ .** a–c,  $\text{Nb}_{16}\text{W}_5\text{O}_{55}$  is built up from blocks of  $4 \times 5$  octahedra with the blocks adjoined forming crystallographic shear planes. d–f,  $\text{Nb}_{18}\text{W}_{16}\text{O}_{93}$  is a  $1 \times 3 \times 1$  superstructure of the tetragonal tungsten bronze with pentagonal tunnels partially filled by  $-\text{W}-\text{O}-$  chains that form pentagonal bipyramids.

$\text{Nb}_{16}\text{W}_5\text{O}_{55}$  is a metastable member within the  $\text{Nb}_2\text{O}_5$ – $\text{WO}_3$  phase diagram<sup>22</sup> with a monoclinic structure comprised of subunits of corner-shared octahedra arranged into  $\text{ReO}_3$ -like blocks, four octahedra wide by five octahedra long, and infinite in the third dimension (Fig. 1a).<sup>23</sup> The block subunits are connected by crystallographic shear planes along the edges and by tetrahedra at each corner leading to the notation  $(4 \times 5)_1$  where, in  $(m \times n)_p$ ,  $m$  and  $n$  denote block length in units of octahedra and  $p$  relates to the connectivity of the blocks which may also be joined in pairs ( $p = 2$ ) or infinite ribbons ( $p = \infty$ ). To the best of our knowledge, this is the first reported application, of any kind, for  $\text{Nb}_{16}\text{W}_5\text{O}_{55}$  since its discovery in 1965.<sup>23,24</sup>  $\text{Nb}_{18}\text{W}_{16}\text{O}_{93}$  is orthorhombic, a  $1 \times 3 \times 1$  superstructure of the classic tetragonal tungsten bronze (Fig. 1d, S2). The superstructure<sup>25</sup> results from partial filling of pentagonal tunnels by  $-\text{M}-\text{O}-$  chains to form pentagonal bipyramids in addition to the distorted octahedra of the tetragonal tungsten bronzes.  $\text{Nb}_{16}\text{W}_5\text{O}_{55}$  and  $\text{Nb}_{18}\text{W}_{16}\text{O}_{93}$  were prepared via co-thermal oxidation of pellets of  $\text{NbO}_2$  and  $\text{WO}_2$ . Details and alternative synthetic routes are described in the Methods (Fig. S3–7).

Reaction of  $\text{Nb}_{16}\text{W}_5\text{O}_{55}$  with lithium (Fig. 2a) proceeds in three regions from 2.5 V to 1.0 V, with an average voltage of 1.57 V (Fig. S1), comparable to the average voltage of  $\text{Li}_4\text{Ti}_5\text{O}_{12}$  of 1.55 V<sup>26</sup>. The three regions, more easily observed in the derivative plot (Fig. 2b), are characterized by their slope and are reminiscent of the three regions observed in other crystallographic shear

structures<sup>27</sup>, *e.g.*, H-Nb<sub>2</sub>O<sub>5</sub><sup>28</sup>, PNB<sub>9</sub>O<sub>25</sub><sup>29</sup>, TiNb<sub>2</sub>O<sub>7</sub><sup>30</sup>, and Nb<sub>12</sub>WO<sub>33</sub><sup>31</sup>. When the kinetics were examined over a range of current densities from C/5 (34.3 mA·g<sup>-1</sup>) up to 60C (10.3 A·g<sup>-1</sup>), Nb<sub>16</sub>W<sub>5</sub>O<sub>55</sub> showed unprecedented bulk rate performance in standard electrode formulations (See Methods) (Fig. 2a–b,e, S8). At C/5, around 1.3 Li<sup>+</sup> can be reversibly intercalated per transition metal for a gravimetric capacity of *ca.* 225 mA·h·g<sup>-1</sup>. When the rate is increased by a factor of 25 to 5C, Nb<sub>16</sub>W<sub>5</sub>O<sub>55</sub> maintains a capacity of 1.0 Li<sup>+</sup>/TM (171 mA·h·g<sup>-1</sup>). At 20C, which corresponds to a three minute discharge, it is still possible to exchange 0.86 Li<sup>+</sup>/TM and access 148 mA·h·g<sup>-1</sup>. Rate tests on Nb<sub>16</sub>W<sub>5</sub>O<sub>55</sub> were measured with a potentiostatic hold at the top of charge to ensure a reliable starting point for discharge. To test the performance under more demanding conditions, 1000 cycles were measured with fixed galvanostatic discharge and charge conditions of 10C for 250 cycles followed by 20C for 750 cycles with no voltage hold (Fig. 2f). Under these conditions, 0.90 Li<sup>+</sup>/TM (avg. 155 mA·h·g<sup>-1</sup>) were reversibly intercalated at 10C with 95% capacity retention after 250 cycles on non-optimized or calendared electrodes. At 20C, the capacity was 0.75 Li<sup>+</sup>/TM (avg. 128 mA·h·g<sup>-1</sup>); the capacity retention was again 95% over the 750 cycles at 20C.

In an extension to another niobium tungsten oxide with distinct structural motifs, excellent electrochemical energy storage was also discovered with μm-scale particles of the bronze-like phase Nb<sub>18</sub>W<sub>16</sub>O<sub>93</sub> (Fig. 1c–f), with enhanced rate performance at the highest rates (Fig. 2e–f). The average voltage of Nb<sub>18</sub>W<sub>16</sub>O<sub>93</sub> is 1.67 V (Fig. S1). In terms of gravimetric capacity, Nb<sub>18</sub>W<sub>16</sub>O<sub>93</sub> stores *ca.* 20 mA·h·g<sup>-1</sup> less than Nb<sub>16</sub>W<sub>5</sub>O<sub>55</sub> at C/5 and 1C due to the higher molar mass of the tungsten-rich bronze phase. However, at 20 C, Nb<sub>18</sub>W<sub>16</sub>O<sub>93</sub> is still able to accommodate a full unit Li<sup>+</sup>/TM for a capacity of *ca.* 150 mA·h·g<sup>-1</sup>. At 60C and 100C (14.9 A·g<sup>-1</sup>), the capacity is still 105 and 70 mA·h·g<sup>-1</sup>, respectively.

Other cycling conditions such as long term cycling at C/5 and the effect of current collectors, which cannot be ignored at high rates<sup>32</sup>, were examined (Fig. S9–10). As a control, Li || Li symmetric cells were cycled at current densities corresponding to those for C/5 to 100C in Fig. 2c (Fig. S11). The overpotentials in the symmetric cell closely match those observed in the electrochemical cycling curves of Fig. 2a–d. This suggests that the extremely high rates for a bulk electrode are approaching the limits of Li metal plating/stripping and/or lithium-ion desolvation and transport in carbonate ester electrolytes at room temperature, *i.e.*, a significant fraction of the ohmic drop during fast charging results from the Li metal and electrolyte rather than the complex oxide electrode materials.

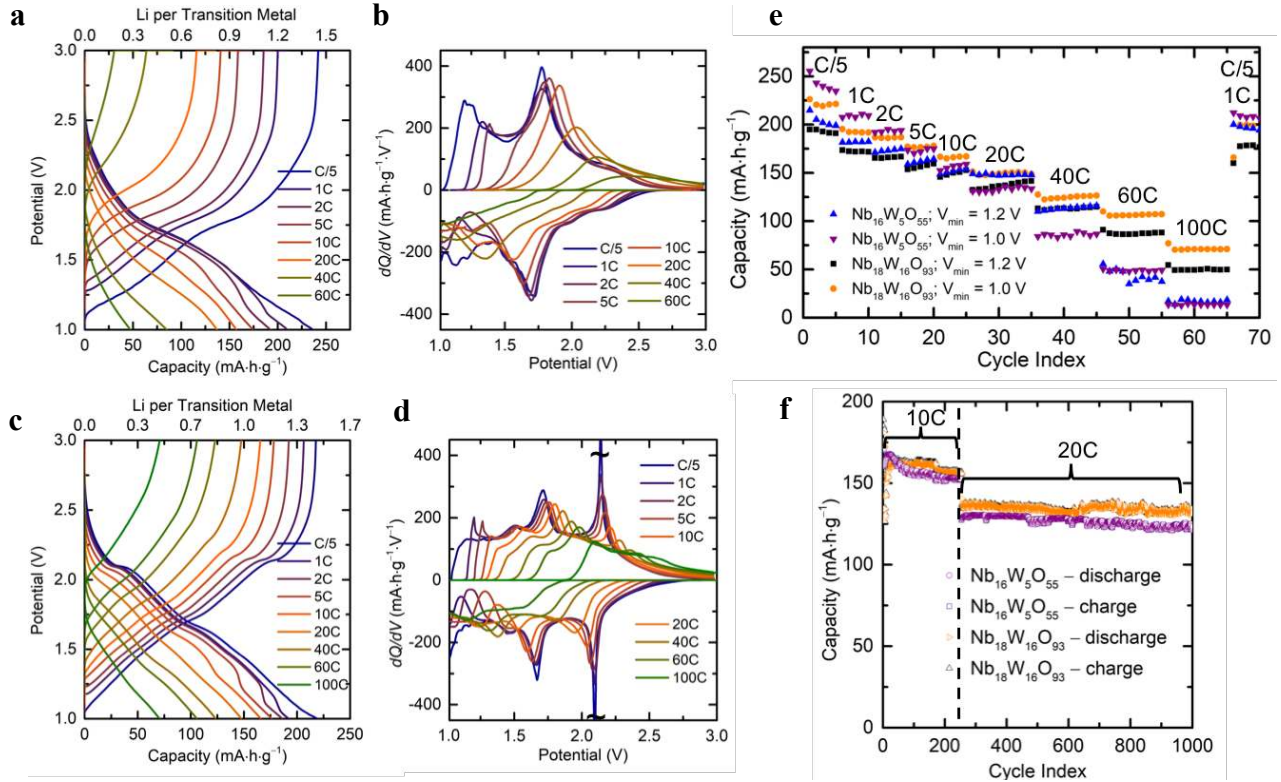


**Figure 2 | Electrochemistry of  $\text{Nb}_{16}\text{W}_5\text{O}_{55}$  and  $\text{Nb}_{18}\text{W}_{16}\text{O}_{93}$ .** Galvanostatic discharge and charge curves and  $dQ/dV$  plots of bulk **a–b**,  $\text{Nb}_{16}\text{W}_5\text{O}_{55}$  and **c–d**,  $\text{Nb}_{18}\text{W}_{16}\text{O}_{93}$  from C/5 to 100C. **e**, Rate performance summary based on gravimetric capacity. **f**, High-rate cycling of 250 cycles at 10C followed by 750 cycles at 20C. Dense electrodes of large particles with  $2\text{--}3\text{ mg}\cdot\text{cm}^{-2}$  active mass loading were tested at current densities corresponding to discharge times of several hours to tens of seconds.  $\text{Nb}_{16}\text{W}_5\text{O}_{55}$  was charged with a 1 h constant voltage step at the top of charge to ensure a comparable starting point on discharge;  $\text{Nb}_{18}\text{W}_{16}\text{O}_{93}$  was cycled without this step and stored over  $100\text{ mA}\cdot\text{h}\cdot\text{g}^{-1}$  at 60C (i.e., in  $<60\text{ s}$ ). High-rate cycling for 1000 cycles was performed on both oxides at 10C/20C constant current without any potentiostatic step.

The extremely high mobility of  $\text{Li}^+$  ions in these systems enabled the direct measurement of lithium diffusion with the pulsed field gradient (PFG) NMR technique, which has previously only been performed on liquids or diamagnetic superionic solid electrolytes (Table S2). To combat the short  $T_2$  (spin–spin) relaxation times of the Li ions, which generally prevent these measurements in electrode materials, experiments were performed from 333–453 K. Analysis of the data (Fig. S12–14, Methods and Supplementary Text) for  $\text{Li}_x\text{Nb}_{16}\text{W}_5\text{O}_{55}$  ( $x = 6.3, 8.4$ ) and  $\text{Li}_x\text{Nb}_{18}\text{W}_{16}\text{O}_{93}$  ( $x = 3.4, 6.8, 10.2$ ) showed lithium transport above  $10^{-13}\text{ m}^2\cdot\text{s}^{-1}$  at 333 K and  $10^{-12}\text{ m}^2\cdot\text{s}^{-1}$  at 373 K. Assuming Arrhenius behavior, and the extremely low measured activation energies of 0.10–0.30 eV, the room temperature lithium diffusion coefficients are estimated to be  $> 1\times 10^{-13}\text{ m}^2\cdot\text{s}^{-1}$  for all the materials (Table 1). The different samples exhibited similar diffusion coefficients and activation energies, consistent with the transport measurements made via the use of the galvanostatic intermittent titration technique (GITT) (Supplementary Materials; Fig. S15) at low to moderate lithium contents. Lithium diffusion in both niobium tungsten oxide structures is

markedly faster than that of  $\text{Li}_{4+x}\text{Ti}_5\text{O}_{12}$  or  $\text{Li}_x\text{TiO}_2$  at *ca.*  $10^{-16}$ – $10^{-15}$   $\text{m}^2\cdot\text{s}^{-1}$  and is close to the best known lithium solid electrolytes (Table S2). GITT (Fig. S15) and PFG NMR (Fig. S12) results indicate that this rapid motion is maintained to high lithium contents ( $\geq 1.5$   $\text{Li}^+/\text{TM}$ ) where the diffusion then drops by about two orders-of-magnitude toward 2.0  $\text{Li}^+/\text{TM}$ . These complementary techniques suggest that the inherent range of the niobium tungsten oxide electrode materials for high-rate multi-redox extends to approximately 1.5  $\text{Li}^+/\text{TM}$ . The diffusion coefficients on the order of  $10^{-12}$ – $10^{-13}$   $\text{m}^2\cdot\text{s}^{-1}$  measured for these materials are consistent with the values required to achieve full lithiation of 10  $\mu\text{m}$  particles on a 60C timescale (Table S3).

**Table 1. Lithium diffusion coefficients from PFG NMR.**

Component	$D_{\text{Li}}$ ( $\text{m}^2\cdot\text{s}^{-1}$ ) @ 298 K	$D_{\text{Li}}$ ( $\text{m}^2\cdot\text{s}^{-1}$ ) @ 413 K	$E_a$ (eV)
$\text{Li}_{6.3}\text{Nb}_{16}\text{W}_5\text{O}_{55}$ - <i>a</i> (15%)	$2.1 \times 10^{-12}$	$2.7 \times 10^{-11}$	$0.23 \pm 0.04$
$\text{Li}_{6.3}\text{Nb}_{16}\text{W}_5\text{O}_{55}$ - <i>b</i> (85%)	$1.7 \times 10^{-13}$	$5.2 \times 10^{-13}$	$0.10 \pm 0.04$
$\text{Li}_{8.4}\text{Nb}_{16}\text{W}_5\text{O}_{55}$	$1.6 \times 10^{-13}$	$6.5 \times 10^{-13}$ (403 K)	$0.13 \pm 0.01$
$\text{Li}_{3.4}\text{Nb}_{18}\text{W}_{16}\text{O}_{93}$	$1.1 \times 10^{-13}$	$2.0 \times 10^{-12}$	$0.27 \pm 0.03$
$\text{Li}_{6.8}\text{Nb}_{18}\text{W}_{16}\text{O}_{93}$	$1.1 \times 10^{-13}$	$1.8 \times 10^{-12}$	$0.30 \pm 0.01$
$\text{Li}_{10.2}\text{Nb}_{18}\text{W}_{16}\text{O}_{93}$	$1.1 \times 10^{-13}$	$2.7 \times 10^{-12}$	$0.29 \pm 0.01$

$D_{\text{Li}}$  was measured directly from 333–453 K and extrapolated from the activation energy to room temperature where the  $T_2$  relaxation was too short to allow direct measurement. Error estimates for activation energies are derived from the standard error of the linear fit. Error bars for the diffusion coefficients are given in Fig. S12. The two diffusion components observed in  $\text{Li}_{6.3}\text{Nb}_{16}\text{W}_5\text{O}_{55}$  are denoted as *a* and *b* with 15% and 85% signal contribution, respectively.

In order to understand (i) the nature of the charge transfer sequence as a function of lithiation and (ii) the origin of multielectron redox behavior in  $\text{Nb}_{16}\text{W}_5\text{O}_{55}$  and  $\text{Nb}_{18}\text{W}_{16}\text{O}_{93}$ , the X-ray absorption near-edge structure (XANES) of the Nb *K*-edge and W *L*-edges was analyzed (Fig. S16, Supplementary Text). For  $\text{Nb}_{16}\text{W}_5\text{O}_{55}$ , *operando* and *ex situ* Nb *K*-edge XANES spectra show a nearly linear trend between the number of electrons (*i.e.*  $\text{Li}^+$ ) transferred and the oxidation state of niobium, extracted from the shift of the absorption edge (Fig. 3a, S17–18). Similarly, *ex situ* samples measured at the W *L*<sub>II,III</sub>-edges show a steadily negative correlation between capacity and edge position but there appears to be a larger shift in the tungsten absorption edge for the first 0.5  $\text{Li}^+/\text{TM}$  inserted (Fig. 3b, S17, S19–20), indicating a slight preference for tungsten reduction initially. The situation for  $\text{Nb}_{18}\text{W}_{16}\text{O}_{93}$  (Fig. 3, S17, S21–23) is analogous in that the niobium oxidation state decreases nearly linearly and tungsten reduction is slightly favored initially; however, there is a clear preference for multielectron reduction to occur on the tungsten throughout lithiation with  $\text{Nb}^{3+}$  appearing only beyond 1.5  $\text{Li}^+/\text{TM}$ .

The redox centers  $\text{Nb}^{5+}$  and  $\text{W}^{6+}$  in  $\text{Nb}_{16}\text{W}_5\text{O}_{55}$  are both  $d^0$  and both of the cations located in 6-coordinate environments experience second-order Jahn–Teller (SOJT) distortions, which give rise to a pre-edge feature before the main absorption edge in Nb *K*- and W *L*<sub>I</sub>-edge XAS spectra (Fig. S18, S20–21, S23–25); this serves as a direct probe of local symmetry and an additional measure of oxidation state. As the  $d^0$  cations are reduced, the energy of the *d*-states moves up and the SOJT distortion is reduced, which increases the local octahedral symmetry and decreases the pre-edge states and intensity monotonically (Fig. 3c, S18, S20–21, S23–24),<sup>23</sup> again with a slightly larger effect on tungsten at low lithium concentrations and a bigger difference between tungsten and



niobium in  $\text{Nb}_{18}\text{W}_{16}\text{O}_{93}$ . By *ca.* 0.8–1.0  $\text{Li}^+/\text{TM}$ , both the Nb  $K$  and W  $L_I$  distinct pre-edges of both the block and bronze phase have decreased and reached a plateau, lithiation thus being associated with an increase in local symmetry for the  $d^0$  oxide intercalation hosts.

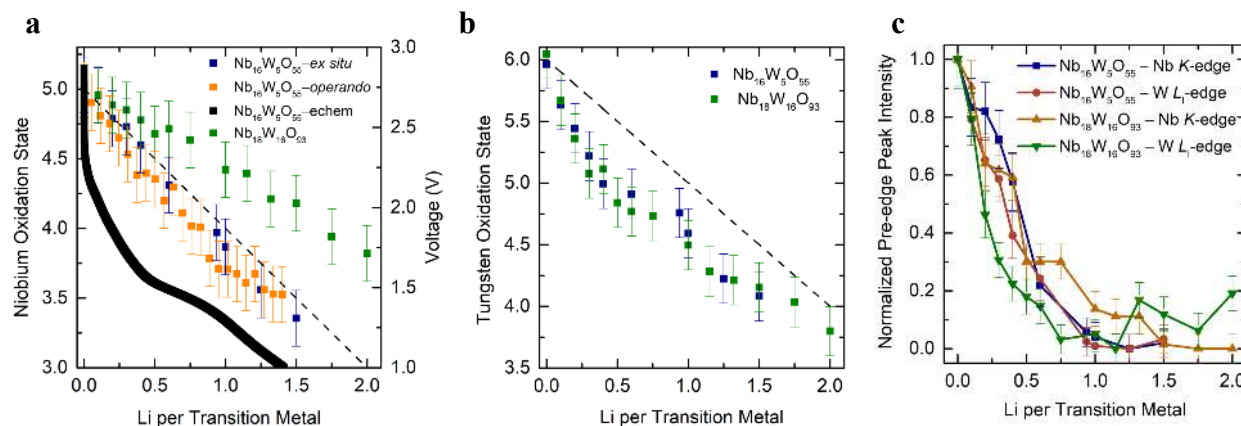


**Figure 3 | X-ray absorption spectroscopy of  $\text{Nb}_{16}\text{W}_5\text{O}_{55}$  and  $\text{Nb}_{18}\text{W}_{16}\text{O}_{93}$ .** **a**, Niobium and **b**, tungsten oxidation states, as a function of lithiation, extracted from shifts in the absorption energy of the Nb  $K$ -edge and W  $L_{II}$ -edge. The black dashed line demarcates a slope of negative one, for reference. **c**, Pre-edge integrated peak intensity from the Nb  $K$ -edge and W  $L_I$ -edge serves as a measure of local distortion from SOJT effects on  $d^0$  octahedral sites and, as the SOJT effect is relaxed upon reduction to  $d^1$  (see Supplementary Materials for discussion), a further indication of oxidation state.

To probe the lattice evolution of these complex oxides upon lithiation, *operando* synchrotron X-ray diffraction was performed at different cycling rates. At C/2,  $\text{Nb}_{16}\text{W}_5\text{O}_{55}$  evolves through a complex, three-stage solid-solution mechanism (Fig. 4a,c, S26–28) that correlates with the observed electrochemical regions: (a) high voltage (until *ca.*  $65 \text{ mA} \cdot \text{h} \cdot \text{g}^{-1}$  or  $0.4 \text{ Li}^+/\text{TM}$ ): *ac*-plane expansion of the blocks along with a slight expansion perpendicular to the block plane, (b) *ca.*  $65$ – $170 \text{ mA} \cdot \text{h} \cdot \text{g}^{-1}$  ( $0.4$ – $1.0 \text{ Li}^+/\text{TM}$ ): anisotropic behavior involving a contraction of the blocks and a significant expansion in the (perpendicular) *b* direction, (c) multiredox (beyond  $1.0 \text{ Li}^+/\text{TM}$ ): linear expansion in all dimensions. The volume expansion is significantly buffered by the block contraction in the second stage and the lattice undergoes only 5.5% expansion at lithiation to  $1.0 \text{ Li}^+/\text{TM}$ . Of note, diffraction shows that the second electrochemical process, though it has a relatively small gradient, is not two-phase, consistent with the GITT measurements (Fig. S15). Upon charge, the stages are reversed (Fig. S29) though there is some first cycle capacity loss. This capacity loss is ascribed at least in part to residual Li remaining in the structure (Fig. S30–31, Table S4), rather than the usual SEI formation, the final lithium ions being significantly harder to extract as their removal would lead to insulating domains. At a factor of ten higher rate (5C), only the first two stages of lattice evolution were observed (Fig. S27–28, 32), which is consistent with the capacity. In addition, there is more strain and reaction inhomogeneity at 5C, consistent with previous *in situ* studies that clearly showed that at these rates, lithium transport within the electrolyte results in internal (electrolyte) inhomogeneities and concentration gradients<sup>33,34</sup>. Nevertheless, the mechanism remains solid-solution, which is evident in the significant interpeak intensity (Fig. S28).

*Operando* diffraction experiments of  $\text{Nb}_{18}\text{W}_{16}\text{O}_{93}$  were performed at rates up to 10C (Fig. 4b,d; S33–37). Like the block phase, the bronze phase shows a complicated but reversible non-linear and strongly anisotropic structural evolution upon lithiation (Fig. 4b, Supplementary Text). Interestingly, the  $b \approx 3a$  pseudo-superstructure relationship persists until the fourth intercalation region at greater than 0.5  $\text{Li}^+/\text{TM}$ . From this point, the unit cell volume actually decreases with increasing lithium intercalation and is the same volume at 1.0  $\text{Li}^+/\text{TM}$  as at 0.5  $\text{Li}^+/\text{TM}$ , a total increase of only 2.8% from the unlithiated host. This is phenomenologically related to negative thermal expansion (NTE)<sup>35,36</sup> or negative linear compressibility (NLC)<sup>37</sup> and may have shared origins related to tilting of the polyhedral units (*vide infra*). The small volume change has implications for the suppression of intergranular cracking and long-term cycle performance<sup>38</sup>. Unlike in the shear structure, the bronze exhibits a compositionally narrow two-phase reaction between approximately  $\text{Li}_{6.6}\text{Nb}_{18}\text{W}_{16}\text{O}_{93}$  and  $\text{Li}_{10.2}\text{Nb}_{18}\text{W}_{16}\text{O}_{93}$  (0.2–0.3  $\text{Li}^+/\text{TM}$ ); the phase transition preserves the *Pbam* space group symmetry but features *ab*-plane expansion and contracted bronze layers. The structural stability of both the block and bronze phases is also reflected in the capacity stability over 1000 discharge–charge cycles (Fig. 2f).



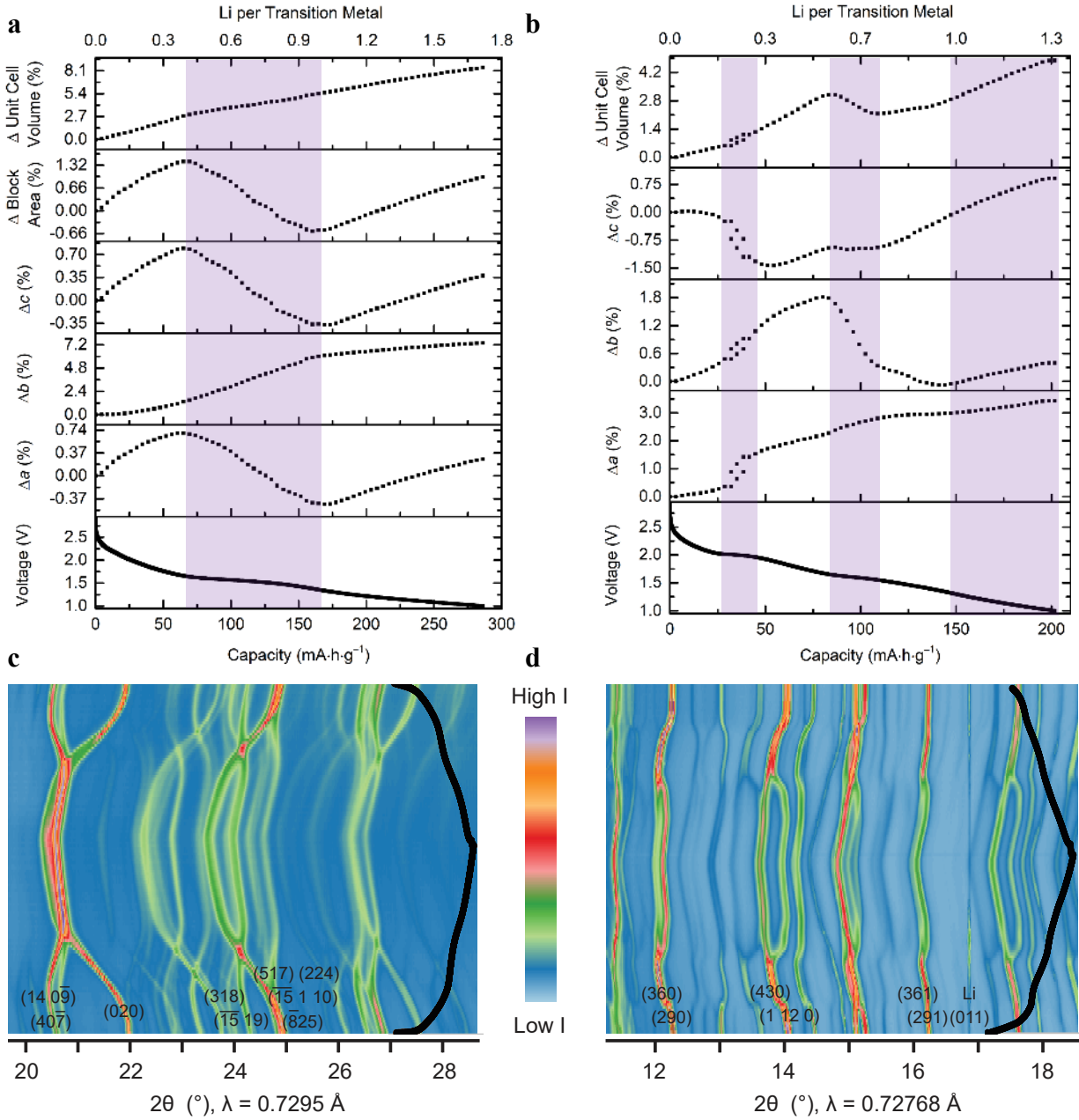


**Figure 4 | Non-linear structural evolution of  $\text{Nb}_{16}\text{W}_5\text{O}_{55}$  and  $\text{Nb}_{18}\text{W}_{16}\text{O}_{93}$  from *operando* synchrotron diffraction.** **a**, The block-phase  $\text{Nb}_{16}\text{W}_5\text{O}_{55}$  evolves in three stages upon lithiation from 3.0–1.0 V at C/2; the expansion is buffered by block contraction in the second stage. **b**, The bronze-like phase  $\text{Nb}_{18}\text{W}_{16}\text{O}_{93}$  evolves through six stages upon lithiation from 3.0–1.0 V at 1C. In this complex oxide, volume expansion is buffered by layer contraction in the second stage (two-phase) and *b*-axis contraction in the fourth and fifth stage. **c**,  $\text{Nb}_{16}\text{W}_5\text{O}_{55}$  and **d**,  $\text{Nb}_{18}\text{W}_{16}\text{O}_{93}$  *operando* diffraction pattern sections with some of the strongest reflections labeled and the electrochemistry overlaid.

Relative to the parent  $\text{ReO}_3$  structure, the niobium tungsten oxides accommodate anion-deficient nonstoichiometry by forming topologically-distinct condensed phases. This has important consequences for Li motion, the intersecting crystallographic shear planes (block phases) or twisted octahedra locked to pentagonal columns (bronze-like) (Fig. 1a,d, S38) decreasing the structural degrees of freedom (See discussion of Parent Structure and rigid unit modes, RUMs, SI). Structural analyses and bond valence energy landscape calculations (Fig. S39), indicate that infinite lithium diffusion in the  $\text{Nb}_{16}\text{W}_5\text{O}_{55}$  block phase is one-dimensional down the  $b$ -axis but the twelve parallel tunnels act as metaphorical multi-lane highways, enabling lithium to change “lanes” via a local hop in the  $ac$ -plane. Lithium sites and diffusion in this twelve-channel path are essentially identical to that of the  $\text{ReO}_3/\text{LLTO}$  structure types (Fig. S39) but without the phase transition of  $\text{ReO}_3$  or the blocking  $\text{La}^{3+}$  ions of LLTO. Furthermore, given this mechanism,  $\text{Nb}_{16}\text{W}_5\text{O}_{55}$  should not be susceptible to the tunnel-blocking defects that hinder micrometer-sized one-dimensional conductors such as  $\text{LiFePO}_4$ .<sup>39–41</sup> Meanwhile, the  $\text{Nb}_{18}\text{W}_{16}\text{O}_{93}$  bronze-like phase has the infinite two-dimensional lithium pathway of high-rate T- $\text{Nb}_2\text{O}_5$  in the  $ab$  crystallographic plane with the additional benefit of four- and five-membered windows and channels along the  $c$ -axis (Fig. S39) to increase the dimensionality of long-range diffusion to 3D. As a result, the structure appears to exhibit better performance, certainly under comparable morphologies and conditions, than the recently intensely studied low temperature T-phase of  $\text{Nb}_2\text{O}_5$ .<sup>11,19,28,42,43</sup> The bronze comparisons stress the complementary benefits of the open room-and-pillar host structure found in T- $\text{Nb}_2\text{O}_5$ <sup>11</sup> and  $\text{Nb}_{18}\text{W}_{16}\text{O}_{93}$  and the additional perpendicular lithium diffusion channels in  $\text{Nb}_{18}\text{W}_{16}\text{O}_{93}$ . In addition, both  $\text{Nb}_{16}\text{W}_5\text{O}_{55}$  and  $\text{Nb}_{18}\text{W}_{16}\text{O}_{93}$  may benefit from the randomly-distributed Nb/W occupancy throughout the metal sites which prevents rate-inhibiting long-range lithium ordering(s).  $\text{Nb}_{16}\text{W}_5\text{O}_{55}$  and  $\text{Nb}_{18}\text{W}_{16}\text{O}_{93}$  are compared to their binary counterparts H- and T- $\text{Nb}_2\text{O}_5$ , respectively, as a function of capacity and  $\text{Li}^+/\text{TM}$  (Fig. S40). Though the niobium tungsten oxide hosts are  $d^0$  insulators, their three-dimensional  $-\text{M}-\text{O}-$  connectivity enables effective electronic pathways as the structure is  $n$ -doped upon lithiation. In addition, variations of the bronze and crystallographic shear structure types are abundant and tunable for specific applications and beyond Li electrochemical energy storage (See Structure Family Extensions, SI).

When compared strictly on the basis of theoretical 1.0  $\text{Li}^+/\text{TM}$  reaction and crystallographic density of the active material, titania, niobia, and graphite all display charge densities of greater than  $800 \text{ A}\cdot\text{h}\cdot\text{L}^{-1}$  (Fig. S41). Once experimental capacities and tap density are considered (Fig. 5a, Table S5), the bulk, unoptimized niobium tungsten oxides presented here maintain volumetric charge densities of greater than  $500 \text{ A}\cdot\text{h}\cdot\text{L}^{-1}$  at 1C and up to  $400 \text{ A}\cdot\text{h}\cdot\text{L}^{-1}$  at 20 C, volumetric performance that even the most optimized versions of  $\text{TiO}_2$ ,  $\text{Nb}_2\text{O}_5$ , LTO cannot achieve. This is not to say that the compounds presented cannot be improved by methods such as nanostructuring, calendaring, or carbon-coating as demonstrated by *e.g.* Duan *et al.* with holey-graphene scaffolds<sup>43</sup> but to prove that large micrometer particles can be used for high-rate electrodes and illustrate that nanosizing is not always the most appropriate strategy to improve performance. This is evident in a Ragone plot (Fig. 5b), which shows the higher energy densities of the new bulk niobium tungsten oxides, as compared to state-of-the-art high-rate anode materials and to graphite.

The ability to intercalate lithium into microscopic particles in minutes, with transport numbers approaching the best liquid and solid electrolytes, calls for a different paradigm for electrode structuring. Rather than focusing on particle dimensions, other aspects such as electrolyte transport or counter electrode diffusivity and overpotential may become more critical to push the frontier of performance. The strict requirements for carbon-coating and intricately wiring nanoparticles are

relaxed and issues stemming from surface reactivity and stability are also diminished. Other applications of these materials can be envisaged. For example, in the field of all-solid-state batteries, there has been a mismatch between lithium transport in solid electrolytes compared to electrode materials. If both components have similar diffusivities, it may be possible to design and implement new, simplified composite structures to speed up the realization of safe all-solid-state cells.

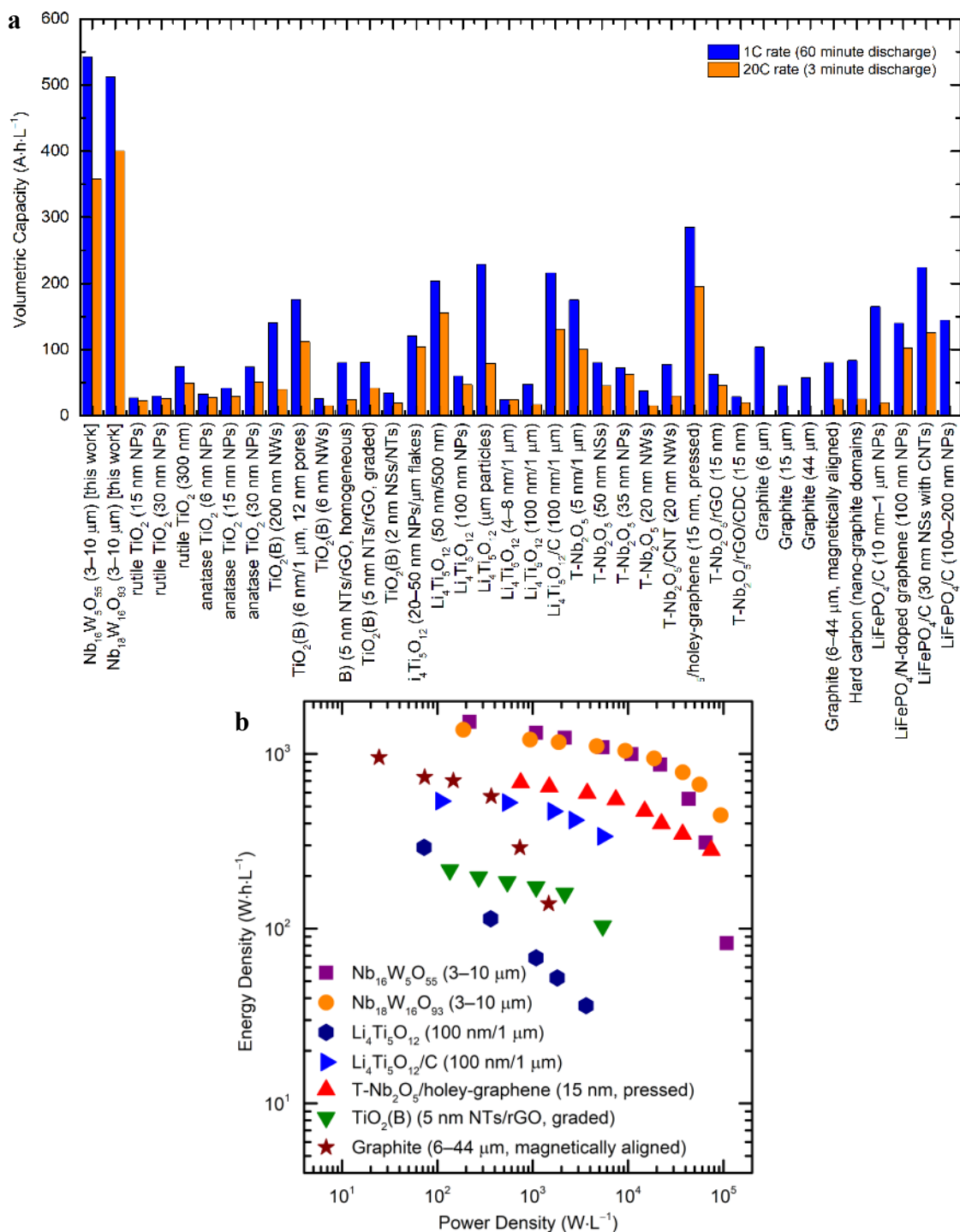


**Figure 5 | Energy and Powder Densities of Micron-sized  $\text{Nb}_{16}\text{W}_5\text{O}_{55}$  and  $\text{Nb}_{18}\text{W}_{16}\text{O}_{93}$  compared to state-of-the-art high rate nanoscale materials and formulations.** **a**,  $\text{Nb}_{16}\text{W}_5\text{O}_{55}$  and  $\text{Nb}_{18}\text{W}_{16}\text{O}_{93}$  from this work are compared to high-rate electrode formulations from the literature. Volumetric capacities at 1C and 20C are determined from reported capacities and reported, measured, or estimated tap densities (Table S5, references therein). **b**, Ragone (log–log) plot of energy density and power density on the basis of anode active materials vs. a 4.0 V cathode (Methods and Table S5). The mass loading of the niobium tungsten oxides here was  $2.6 \text{ mg}\cdot\text{cm}^{-2}$ , the mass loading of the other titanium and niobium-based materials was *ca.*

1 mg·cm<sup>-2</sup>. Graphite is included as a reference, though it suffers from Li plating risks and particle fracture when used at high rates.

In conclusion, extremely high rate performance has been achieved without nanosizing by identifying appropriate three-dimensional oxide crystal structures. The two new electrode materials, Nb<sub>16</sub>W<sub>5</sub>O<sub>55</sub> and Nb<sub>18</sub>W<sub>16</sub>O<sub>93</sub>, effectively use superstructure motifs to provide stable host structures for lithium intercalation with facile and defect-tolerant lithium diffusion and multielectron redox. Volume expansion is mitigated by structural contraction along specific crystallographic axes in response to increased lithium content, which may enable the extended cycling of these large particles<sup>44</sup>. The materials investigated here operate in a similar voltage region to the well-studied and generally considered to be “safe” anode materials LTO and TiO<sub>2</sub>(B). Rather than the route of trying to overcome physical properties (such as ionic and electronic conductivity) extrinsically (by, for example, nanosizing and carbon coating), this discovery underlines that the high-rate, high-capacity properties of the niobium tungsten oxide block and bronze phases presented here are intrinsic to the complex atomic and electronic networks. The path forward for new fast ionic conductors should consider host structures with open yet frustrated topologies (that prevent structural rearrangements that reduce Li transport) and which also contain “disorder” in the sense of a multitude of guest sites for Li<sup>+</sup> and limited interaction between the host and guest (*e.g.*, no strong coupling between the diffusing Li<sup>+</sup> and associated electron, as found in LiFePO<sub>4</sub><sup>45</sup>, or between the Li<sup>+</sup> and the host structure itself) as this leads to a relatively flat potential energy surface with small kinetic diffusion barriers for Li transport. These criteria, leading to extremely high power and energy densities, are satisfied in Nb<sub>16</sub>W<sub>5</sub>O<sub>55</sub> and Nb<sub>18</sub>W<sub>16</sub>O<sub>93</sub> (Fig. 5b) via crystallographic shear and pentagonal columns that prop open the framework structures, and transition metal disorder that prevents Li ordering.

## Acknowledgements

K.J.G. gratefully acknowledges support from The Winston Churchill Foundation of the United States, the Herchel Smith Scholarship, and the Science and Technology Facilities Council Futures Early Career Award. K.J.G and C.P.G thank the EPSRC via the LIBATT grant (EP/P003532/1). L.E.M. was funded by the European Union’s Horizon 2020 – European Union research and innovation program under the Marie Skłodowska–Curie grant agreement No. 750294. We thank Dr. Ieuan Seymour, University of Cambridge, and Prof. Bruce Dunn, University of California, Los Angeles, for fruitful discussions. We thank Drs. Jeremy Skepper and Heather Greer, University of Cambridge, for assistance with the electron microscopy and Dr. Maxim Avdeev, Bragg Institute, for his bond valence sum mapping program. We thank Dr. Olaf Borkiewicz, Advanced Photon Source, Argonne National Laboratory and Alisha Kasam, University of Cambridge for diffraction data reduction scripts. We thank Diamond Light Source for access to beamline B18 (SP14956, SP16387, SP17913) that contributed to the results presented here. This research used resources of the Advanced Photon Source, a U.S. Department of Energy (DOE) Office of Science User Facility operated for the DOE Office of Science by Argonne National Laboratory under Contract No. DE-AC02-06CH11357.

### Author contributions

K.J.G. and C.P.G. conceived the idea. K.J.G. synthesized and characterized the materials and performed the electrochemistry. K.J.G. performed the synchrotron diffraction and absorption experiments and analyzed the data with support from K.M.W. and G.C. L.E.M. and K.J.G. performed the PFG NMR measurements. K.J.G. and C.P.G. wrote the manuscript with input from all coauthors.

### Data availability

The data that support the findings of this study are available from [www.repository.cam.ac.uk](http://www.repository.cam.ac.uk) and the corresponding author upon reasonable request.

### Competing financial interests

The authors declare no competing financial interests.

### References

1. Zhao, K., Pharr, M., Vlassak, J. J. & Suo, Z. Fracture of electrodes in lithium-ion batteries caused by fast charging. *J. Appl. Phys.* **108**, 073517 (2010).
2. Vetter, J. *et al.* Ageing mechanisms in lithium-ion batteries. *J. Power Sources* **147**, 269–281 (2005).
3. Downie, L. E. *et al.* In Situ Detection of Lithium Plating on Graphite Electrodes by Electrochemical Calorimetry. *J. Electrochem. Soc.* **160**, A588–A594 (2013).
4. Kim, C., Norberg, N. S., Alexander, C. T., Kostecki, R. & Cabana, J. Mechanism of Phase Propagation During Lithiation in Carbon-Free Li<sub>4</sub>Ti<sub>5</sub>O<sub>12</sub> Battery Electrodes. *Adv. Funct. Mater.* **23**, 1214–1222 (2013).
5. Wang, C. *et al.* A robust strategy for crafting monodisperse Li<sub>4</sub>Ti<sub>5</sub>O<sub>12</sub> nanospheres as superior rate anode for lithium ion batteries. *Nano Energy* **21**, 133–144 (2016).
6. Odziomek, M. *et al.* Hierarchically structured lithium titanate for ultrafast charging in long-life high capacity batteries. *Nat. Commun.* **8**, 15636 (2017).



7. Oszajca, M. F., Bodnarchuk, M. I. & Kovalenko, M. V. Precisely Engineered Colloidal Nanoparticles and Nanocrystals for Li-Ion and Na-Ion Batteries: Model Systems or Practical Solutions? *Chem. Mater.* **26**, 5422–5432 (2014).
8. Palacin, M. R., Simon, P. & Tarascon, J. M. Nanomaterials for electrochemical energy storage: the good and the bad. *Acta Chim. Slov.* **63**, 417–423 (2016).
9. Wu, H. *et al.* Stable cycling of double-walled silicon nanotube battery anodes through solid-electrolyte interphase control. *Nat. Nanotechnol.* **7**, 310–315 (2012).
10. Kasnatscheew, J. *et al.* A Tutorial into Practical Capacity and Mass Balancing of Lithium Ion Batteries. *J. Electrochem. Soc.* **164**, A2479–A2486 (2017).
11. Griffith, K. J., Forse, A. C., Griffin, J. M. & Grey, C. P. High-Rate Intercalation without Nanostructuring in Metastable Nb<sub>2</sub>O<sub>5</sub> Bronze Phases. *J. Am. Chem. Soc.* **138**, 8888–8899 (2016).
12. Stramare, S., Thangadurai, V. & Weppner, W. Lithium Lanthanum Titanates: A Review. *Chem. Mater.* **15**, 3974–3990 (2003).
13. Shen, L., Zhang, X., Uchaker, E., Yuan, C. & Cao, G. Li<sub>4</sub>Ti<sub>5</sub>O<sub>12</sub> Nanoparticles Embedded in a Mesoporous Carbon Matrix as a Superior Anode Material for High Rate Lithium Ion Batteries. *Adv. Energy Mater.* **2**, 691–698 (2012).
14. Prakash, A. S. *et al.* Solution-Combustion Synthesized Nanocrystalline Li<sub>4</sub>Ti<sub>5</sub>O<sub>12</sub> As High-Rate Performance Li-Ion Battery Anode. *Chem. Mater.* **22**, 2857–2863 (2010).
15. Xu, G. B. *et al.* Highly-crystalline ultrathin Li<sub>4</sub>Ti<sub>5</sub>O<sub>12</sub> nanosheets decorated with silver nanocrystals as a high-performance anode material for lithium ion batteries. *J. Power Sources* **276**, 247–254 (2015).

16. Ren, Y. *et al.* Nanoparticulate TiO<sub>2</sub>(B): An Anode for Lithium-Ion Batteries. *Angew. Chem. Int. Ed.* **51**, 2164–2167 (2012).
17. Liu, H. *et al.* Mesoporous TiO<sub>2</sub>-B Microspheres with Superior Rate Performance for Lithium Ion Batteries. *Adv. Mater.* **23**, 3450–3454 (2011).
18. Beuvier, T. *et al.* TiO<sub>2</sub>(B) Nanoribbons As Negative Electrode Material for Lithium Ion Batteries with High Rate Performance. *Inorg. Chem.* **49**, 8457–8464 (2010).
19. Augustyn, V. *et al.* High-rate electrochemical energy storage through Li<sup>+</sup> intercalation pseudocapacitance. *Nat. Mater.* **12**, 518–522 (2013).
20. Liu, X. *et al.* Urchin-like hierarchical H-Nb<sub>2</sub>O<sub>5</sub> microspheres: synthesis, formation mechanism and their applications in lithium ion batteries. *Dalton Trans.* **46**, 10935–10940 (2017).
21. Lai, C.-H. *et al.* Designing Pseudocapacitance for Nb<sub>2</sub>O<sub>5</sub>/Carbide-Derived Carbon Electrodes and Hybrid Devices. *Langmuir* **33**, 9407–9415 (2017).
22. Roth, R. S. & Waring, J. L. Phase equilibria as related to crystal structure in the system niobium pentoxide-tungsten trioxide. *J. Res. Natl. Bur. Stand.* **70A**, 281–303 (1966).
23. Roth, R. S. & Wadsley, A. D. Multiple phase formation in the binary system Nb<sub>2</sub>O<sub>5</sub>WO<sub>3</sub>. II. The structure of the monoclinic phases WNb<sub>12</sub>O<sub>33</sub> and W<sub>5</sub>Nb<sub>16</sub>O<sub>55</sub>. *Acta Crystallogr.* **19**, 32–38 (1965).
24. Roth, R. S. & Wadsley, A. D. Multiple phase formation in the binary system Nb<sub>2</sub>O<sub>5</sub>–WO<sub>3</sub>. I. Preparation and identification of phases. *Acta Crystallogr.* **19**, 26–32 (1965).
25. Stephenson, N. C. A structural investigation of some stable phases in the region Nb<sub>2</sub>O<sub>5</sub>.WO<sub>3</sub>–WO<sub>3</sub>. *Acta Crystallogr. B* **24**, 637–653 (1968).

26. Naoi, K., Ishimoto, S., Isobe, Y. & Aoyagi, S. High-rate nano-crystalline  $\text{Li}_4\text{Ti}_5\text{O}_{12}$  attached on carbon nano-fibers for hybrid supercapacitors. *J. Power Sources* **195**, 6250–6254 (2010).
27. Cava, R. J., Murphy, D. W. & Zahurak, S. M. Lithium Insertion in Wadsley-Roth Phases Based on Niobium Oxide. *J. Electrochem. Soc.* **130**, 2345–2351 (1983).
28. Kumagai, N., Koishikawa, Y., Komaba, S. & Koshiba, N. Thermodynamics and Kinetics of Lithium Intercalation into  $\text{Nb}_2\text{O}_5$  Electrodes for a 2 V Rechargeable Lithium Battery. *J. Electrochem. Soc.* **146**, 3203–3210 (1999).
29. Patoux, S., Dolle, M., Rousse, G. & Masquelier, C. A Reversible Lithium Intercalation Process in an  $\text{ReO}_3$  -Type Structure  $\text{PNb}_9\text{O}_{25}$ . *J. Electrochem. Soc.* **149**, A391–A400 (2002).
30. Han, J.-T., Huang, Y.-H. & Goodenough, J. B. New Anode Framework for Rechargeable Lithium Batteries. *Chem. Mater.* **23**, 2027–2029 (2011).
31. Saritha, D., Pralong, V., Varadaraju, U. V. & Raveau, B. Electrochemical Li insertion studies on  $\text{WNb}_{12}\text{O}_{33}$ —A shear  $\text{ReO}_3$  type structure. *J. Solid State Chem.* **183**, 988–993 (2010).
32. Griffith, K. J., Senyshyn, A. & Grey, C. P. Structural Stability from Crystallographic Shear in  $\text{TiO}_2$ – $\text{Nb}_2\text{O}_5$  Phases: Cation Ordering and Lithiation Behavior of  $\text{TiNb}_{24}\text{O}_{62}$ . *Inorg. Chem.* **56**, 4002–4010 (2017).
33. Roberts, M. R. *et al.* Direct Observation of Active Material Concentration Gradients and Crystallinity Breakdown in  $\text{LiFePO}_4$  Electrodes During Charge/Discharge Cycling of Lithium Batteries. *J. Phys. Chem. C* **118**, 6548–6557 (2014).
34. Strobridge, F. C. *et al.* Unraveling the Complex Delithiation Mechanisms of Olivine-Type Cathode Materials,  $\text{LiFe}_x\text{Co}_{1-x}\text{PO}_4$ . *Chem. Mater.* **28**, 3676–3690 (2016).

35. Mary, T. A., Evans, J. S. O., Vogt, T. & Sleight, A. W. Negative Thermal Expansion from 0.3 to 1050 Kelvin in  $\text{ZrW}_2\text{O}_8$ . *Science* **272**, 90–92 (1996).
36. Lin, K. *et al.* Ordered Structure and Thermal Expansion in Tungsten Bronze  $\text{Pb}_2\text{K}_{0.5}\text{Li}_{0.5}\text{Nb}_5\text{O}_{15}$ . *Inorg. Chem.* **53**, 9174–9180 (2014).
37. Cairns, A. B. & Goodwin, A. L. Negative linear compressibility. *Phys. Chem. Chem. Phys.* **17**, 20449–20465 (2015).
38. Liu, H. *et al.* Intergranular Cracking as a Major Cause of Long-Term Capacity Fading of Layered Cathodes. *Nano Lett.* **17**, 3452–3457 (2017).
39. Islam, M. S., Driscoll, D. J., Fisher, C. A. J. & Slater, P. R. Atomic-Scale Investigation of Defects, Dopants, and Lithium Transport in the  $\text{LiFePO}_4$  Olivine-Type Battery Material. *Chem. Mater.* **17**, 5085–5092 (2005).
40. Dathar, G. K. P., Sheppard, D., Stevenson, K. J. & Henkelman, G. Calculations of Li-Ion Diffusion in Olivine Phosphates. *Chem. Mater.* **23**, 4032–4037 (2011).
41. Liu, H. *et al.* Effects of Antisite Defects on Li Diffusion in  $\text{LiFePO}_4$  Revealed by Li Isotope Exchange. *J. Phys. Chem. C* **121**, 12025–12036 (2017).
42. Zhang, C. *et al.* Synthesis and Charge Storage Properties of Hierarchical Niobium Pentoxide/Carbon/Niobium Carbide (MXene) Hybrid Materials. *Chem. Mater.* **28**, 3937–3943 (2016).
43. Sun, H. *et al.* Three-dimensional holey-graphene/niobia composite architectures for ultrahigh-rate energy storage. *Science* **356**, 599–604 (2017).
44. Zhang, S. Chemomechanical modeling of lithiation-induced failure in high-volume-change electrode materials for lithium ion batteries. *Npj Comput. Mater.* **3**, 7 (2017).

45. Maxisch, T., Zhou, F. & Ceder, G. Ab initio study of the migration of small polarons in olivine  $\text{Li}_x\text{FePO}_4$  and their association with lithium ions and vacancies. *Phys. Rev. B* **73**, 104301 (2006).